WILEY

RESEARCH ARTICLE

Regional multimodal relationships between tau, hypometabolism, atrophy, and fractional anisotropy in atypical Alzheimer's disease

Irene Sintini[1] | Christopher G. Schwarz[1] | Peter R. Martin[2] | Jonathan Graff-Radford[3] |
Mary M. Machulda[4] | Matthew L. Senjem[1,5] | Robert I. Reid[5] | Anthony J. Spychalla[1] |
Daniel A. Drubach[3] | Val J. Lowe[1] | Clifford R. Jack Jr[1] | Keith A. Josephs[3] |
Jennifer L. Whitwell[1]

[1]Department of Radiology, Mayo Clinic, Rochester, Minnesota

[2]Department of Health Science Research (Biostatistics), Mayo Clinic, Rochester, Minnesota

[3]Department of Neurology, Mayo Clinic, Rochester, Minnesota

[4]Department of Psychiatry and Psychology, Mayo Clinic, Rochester, Minnesota

[5]Department of Information Technology, Mayo Clinic, Rochester, Minnesota

Correspondence
Irene Sintini, PhD, Department of Radiology, Mayo Clinic, 200 1st St SW, Rochester, MN 55905.
Email: sintini.irene@mayo.edu

Funding information
National Institutes of Health, Grant/Award Numbers: U01-AG006786, R21-NS94684, R01-AG50603

Abstract

Alzheimer's disease (AD) can present with atypical clinical forms where the prominent domain of deficit is not memory, that is, atypical AD. Atypical AD patients show cortical atrophy on MRI, hypometabolism on [18F]fluorodeoxyglucose (FDG) PET, tau uptake on [18F]AV-1451 PET, and white matter tract degeneration on diffusion tensor imaging (DTI). How these disease processes relate to each other locally and distantly remains unclear. We aimed to examine multimodal neuroimaging relationships in individuals with atypical AD, using univariate and multivariate techniques at region- and voxel-level. Forty atypical AD patients underwent MRI, FDG-PET, tau-PET, beta-amyloid PET, and DTI. Patients were all beta-amyloid positive. Partial Pearson's correlations were performed between tau and FDG standardized uptake value ratios, gray matter MRI-volumes and white matter tract fractional anisotropy. Sparse canonical correlation analysis was applied to identify multivariate relationships between the same quantities. Voxel-level associations across modalities were also assessed. Tau showed strong local negative correlations with FDG metabolism in the occipital and frontal lobes. Tau in frontal and parietal regions was negatively associated with temporoparietal gray matter MRI-volume. Fractional anisotropy in a set of posterior white matter tracts, including the splenium of the corpus callosum, cingulum, and posterior thalamic radiation, was negatively correlated with parietal and occipital tau, atrophy and, predominantly, with hypometabolism. These results support the view that tau is the driving force behind neurodegeneration in atypical AD, and that a breakdown in structural connectivity is related to cortical neurodegeneration, particularly hypometabolism.

KEYWORDS

atypical Alzheimer's disease, DTI, FDG, MRI, multimodal imaging, multivariate analysis, tau

1 | INTRODUCTION

Alzheimer's disease (AD) is a progressive neurodegenerative disorder characterized pathologically by the deposition of beta-amyloid (Aβ) in senile plaques and tau in neurofibrillary tangles (Braak & Braak, 1991). Patients with AD dementia typically present with early and prominent episodic memory impairment. However, clinical and pathological studies showed that up to 38% of AD patients under the age of 60 (Balasa

et al., 2011) and 25% of all AD patients (Whitwell et al., 2012) do not present with early memory loss, but instead have other cognitive impairments that typically originate in the cortex. This group of patients is considered to have atypical AD. Patients with atypical AD can present with impairments in language and in visuospatial/visuo-perceptual abilities, executive dysfunction, or praxis (Galton, Patterson, Xuereb, & Hodges, 2000). On neuroimaging, atypical AD patients tend to show a relative sparing of the medial temporal lobes

compared with typical AD (Galton et al., 2000; Madhavan et al., 2013; Whitwell et al., 2007), and instead show patterns of neurodegeneration and tau uptake affecting the cortex (Whitwell et al., 2018), particularly the temporal, parietal and occipital lobes (Dronse et al., 2017; Nasrallah et al., 2018; Ossenkoppele et al., 2016; Tetzloff et al., 2018; Whitwell et al., 2011; Xia et al., 2017).

Different pathophysiological aspects of atypical AD can be captured by different neuroimaging modalities, such as gray matter atrophy with structural magnetic resonance imaging (MRI), tau protein deposition with [18F]AV-1451 positron emission tomography (PET), Aβ protein deposition with [11C]Pittsburgh compound B (PiB) PET, hypometabolism with [18F]fluorodeoxyglucose (FDG) PET, and white matter tract degeneration with diffusion tensor imaging (DTI). Multimodal neuroimaging analyses, combining measurements from MRI, PET, and DTI, allow for an in vivo investigation of the relationships between atrophy, protein deposition, glucose hypometabolism, and white matter disruption at the regional- and voxel-level. This knowledge is essential to understand the causes of neurodegeneration and inform new treatments tailored to address the pathophysiology of the disease. Studies have suggested that the regional pattern of Aβ deposition is consistent across clinical phenotypes of AD and is not related to neurodegeneration (Bischof et al., 2016; Iaccarino et al., 2018; La Joie et al., 2012; Ossenkoppele et al., 2015, 2016; Rabinovici et al., 2008), while tau topographically matches gray matter atrophy and glucose hypometabolism and can therefore be interpreted as the likely driving force behind neurodegeneration (Dronse et al., 2017; Ossenkoppele et al., 2016; Whitwell et al., 2018; Xia et al., 2017). Additionally, it has been observed that AD pathological proteins may spread along functional brain networks, with strongly connected regions displaying a higher tau burden (Cope et al., 2018; Hoenig et al., 2018; Jones et al., 2017) and amyloid being a partial mediator between functional network failure and tau deposition (Jones et al., 2017). The majority of these studies have assessed the spectrum of AD clinical presentations, including both typical and atypical variants. However, it has become increasingly clear that pathophysiological relationships in atypical AD likely differ from typical AD, with other comorbidities and pathologies contributing to the clinical phenotype in late-onset typical AD. We have previously demonstrated that the topographic relationship between tau uptake on [18F]AV-1451 PET and both atrophy and hypometabolism is stronger in younger AD patients and in patients with atypical clinical presentations (Whitwell et al., 2018). However, little is known about regional relationships between the different pathophysiological aspects of the disease in atypical AD. Furthermore, white matter tract degeneration has been observed in atypical AD (Caso et al., 2015; Galantucci et al., 2011; Madhavan et al., 2016; Mahoney et al., 2013; Migliaccio et al., 2012), but how its regional patterns relate to tau deposition and markers of neurodegeneration in atypical AD has not been investigated. Understanding these relationships may help shed light on the underlying mechanisms of white matter damage in atypical AD.

Correlation maps offer an easily interpretable way to observe how one disease process relates to another, both locally and distantly. However, univariate analysis methods present some limitations, such as the considerable number of multiple comparisons necessary to directly assess such correlations and the high computational cost

(Avants et al., 2014). Multivariate methods can be implemented to overcome such limitations in high dimensional datasets. Sparse canonical correlation analysis (SCCA) is an unsupervised multivariate method that estimates the linear relationship between two set of variables by projecting them onto dimensions where they are maximally correlated to each other (Witten, Tibshirani, & Hastie, 2009). In the projection onto the canonical dimensions, each variable is assigned a coefficient called canonical weight. Unlike the classic canonical correlation analysis (Hotelling, 1936), the sparse version limits the number of variables that can contribute to the canonical dimensions, that is, to the maximized correlation, and it is therefore well suited when the number of such variables is large and possibly larger than the number patients. SCCA has been implemented in neuroimaging to compute spatially disjoint multivariate associations (Adams, Lockhart, Li, & Jagust, 2018; Avants, Cook, Ungar, Gee, & Grossman, 2010; Avants et al., 2014), identifying mutually predictive anatomical regions between different modalities. In addition to combining univariate and multivariate techniques, combining regions-of-interest (ROI)- and voxel-level analyses offers a wider perspective for characterizing the associations between multimodal neuroimaging biomarkers (Wirth et al., 2018).

We aimed to describe cross-sectional regional relationships between tau-PET uptake, gray matter atrophy, glucose hypometabolism, and white matter tract degeneration (measured using fractional anisotropy [FA]) in a cohort of 40 atypical AD patients, using complementary univariate and multivariate techniques, at the regional- and voxel-level. We hypothesized that tau would be the driving factor for local measures of neurodegeneration, that is, hypometabolism and atrophy, and therefore we expected strong local associations among these quantities. In addition, we expected to highlight associations between degeneration of white matter tracts that are connected to the regions of the brain most involved in the disease. We did not investigate spatial relationships involving Aβ-PET uptake, since the population of patients we analyzed was at an advanced stage of the disease and therefore the already widespread amyloid was unlikely to reveal spatial association with the other imaging modalities. Indeed, other studies already highlighted the absence of regional associations between Aβ deposition and neurodegeneration (Iaccarino et al., 2018; Ossenkoppele et al., 2015, 2016) or even a mild opposite trend between the two (Bischof et al., 2016).

2 | METHODS

2.1 | Participants

Patients were recruited from the Mayo Clinic Department of Neurology into an NIH-funded study assessing atypical AD (PI Whitwell). We recruited patients meeting clinical criteria for posterior cortical atrophy (PCA) (Crutch et al., 2012) and for the logopenic variant of primary progressive aphasia (lvPPA) (Gorno-Tempini et al., 2008). All patients underwent structural MRI, DTI, tau-PET, and Aβ-PET. We selected patients (n = 40) with Aβ deposition on Aβ-PET (n = 20 diagnosed with PCA, n = 20 diagnosed with lvPPA). Among these patients, 31 also underwent FDG-PET. All patients underwent a comprehensive

neurological evaluation by a Behavioral Neurologist (KAJ or JGR), details of which can be found in a previous study (Tetzloff et al., 2018). The demographic and clinical features of the cohort are shown in Table 1. The study was approved by the Mayo Clinic IRB, and all patients consented to participate in this study.

2.2 | Image acquisition

All PET scans were acquired using a PET/CT scanner (GE Healthcare, Milwaukee, Wisconsin) operating in 3D mode. For tau-PET, an intravenous bolus injection of approximately 370 MBq (range 333–407 MBq) of [18F]AV-1451 was administered, followed by a

TABLE 1 Demographic and clinical features of the atypical AD patients

	lvPPA (N = 20)	PCA (N = 20)	Total (N = 40)
Demographics			
Female sex	14 (70.0%)	14 (70.0%)	28 (70.0%)
Education (years)	16 (14, 16)	16 (12, 18)	16 (14, 16)
Age at onset (years)	65 (58, 71)	57 (54, 63)	62 (56, 66)
Early-onset patients (before 65 years)	8 (40.0%)	16 (80.0%)	24 (60.0%)
Age at MRI[a] (years)	68 (61, 74)	65 (60, 70)	67 (60, 72)
Disease duration (years)	2 (2, 3)	4 (3, 6)	3 (2, 5)
Handedness	4 (20.0%)	2 (10.0%)	6 (15.0%)
Global PiB	2.44 (2.18, 2.90)	2.44 (2.26, 2.54)	2.44 (2.19, 2.73)
Neurological evaluation			
MoCA	19 (17, 21)	16 (12, 22)	18 (13, 22)
CDR	2 (1, 3)	4 (2, 9)	3 (2, 5)
NPI-Q	2 (0, 3)	3 (1, 8)	2 (0, 5)
MDS-UPDRS III	2 (2, 4)	1 (0, 7)	2 (1, 5)
Optic ataxia	0 (0.0%)	7 (38.9%)	7 (18.4%)
Oculomotor apraxia	0 (0.0%)	7 (38.9%)	7 (18.9%)
Praxis	58 (56, 60)	60 (55, 60)	59 (56, 60)
Gerstmann	2 (11.1%)	11 (57.9%)	13 (35.1%)
Simultanagnosia	18 (17, 20)	7 (3, 13)	17 (8, 18)
Neuropsychological evaluation			
WMS-III VR % ret. MOANS	9 (6, 11)	8 (6, 9)	8 (6, 10)
Repetition Boston diagnostic	7 (6, 8)	8 (6, 9)	8 (6, 8)
BNT	11 (7, 12)	12 (8, 14)	11 (8, 13)
Letter fluency sum	28 (22, 32)	32 (25, 43)	29 (22, 35)
Animal fluency	10 (8, 14)	11 (6, 16)	10 (7, 15)
VOSP letters (/20)	19 (18, 20)	14 (3, 18)	18 (14, 19)
Rey-O MOANS	6 (2, 10)	2 (2, 2)	2 (2, 6)

MoCA = Montreal cognitive assessment battery; CDR = clinical dementia rating; NPI-Q = neuropsychiatric inventory questionnaire; MSD-UPDRS III = Movement Disorder Society Unified Parkinson's Disease Rating Scale Part III; WMS-III VR% retention MOANS = Wechsler Memory Scale-III Visual Reproduction MOANS (mean: 10 = standard deviation: 3); BNT = Boston naming test; VOSP letters = visual object and space perception battery; Rey-O MOANS = Rey Osterrieth Mayo Older American Normative scale (mean: 10, standard deviation: 3).
Data are shown as Median (25th percentile, 75th percentile).
[a] Age at MRI is identical to age at time of assessment.

20 min PET acquisition performed 80 min after injection. For Aβ-PET, participants were injected with PiB of approximately 628 MBq (range, 385–723 MBq) and, after a 40–60 min uptake period, a 20 min PiB scan was obtained. Both PiB and [18F]AV-1451 scans consisted of four 5-min dynamic frames following a low dose CT transmission scan. Tau-PET and Aβ-PET were performed on the same day for all the patients except one, for whom Aβ-PET was performed 21 days after tau-PET. For FDG-PET, patients were injected with [18F]FDG of approximately 459 MBq (range 367–576 MBq) and, after a 30-min uptake period, an 8-min FDG-PET scan was acquired consisting of four 2-min dynamic frames following a low dose CT transmission scan. Standard corrections were applied. Emission data were reconstructed into a 256 × 256 matrix with a 30-cm FOV (pixel size = 1.0 mm, slice thickness = 1.96 mm). All patients had the FDG-PET scan performed within 1 day from the Aβ and tau-PET scans, except for 10 patients who had the FDG-PET scan within 3.6 months, on average, from the Aβ-PET scan (range: 7 days to 9 months). All participants underwent a 3 T head MRI protocol performed on the same day as the tau-PET scan, except one participant who had the MRI 2 months after the tau-PET. The MRI protocol included (1) a magnetization prepared rapid gradient echo (MPRAGE) sequence TR/TE/TI, 2,300/3/900 ms; flip angle 8°, 26-cm field of view (FOV); 256 × 256 in-plane matrix with a phase FOV of 0.94, and slice thickness of 1.2 mm (Jack et al., 2008), and (2) a DTI acquisition consisting of a single shot echo-planar (EPI) pulse sequence in the axial plane, with approximate TE 64 ms; TR = 10 s; in-plane matrix 128/128; FOV 35 cm; phase FOV 0.66; 41 diffusion encoding directions and five nondiffusion weighted ($b = 0$) T2 images; slice thickness 2.7 mm (2.7 mm isotropic resolution); parallel imaging with a SENSE factor of two was used.

2.3 | Image processing

All PET images were registered to the patients' MPRAGE using 6 degrees-of-freedom rigid body registration. Normalization parameters were computed between each MPRAGE and the Mayo Clinic Adult Lifespan Template (MCALT) (https://www.nitrc.org/projects/mcalt/) using ANTs (Avants, Epstein, Grossman, & Gee, 2008). With these parameters, the MCALT atlas was propagated to the native MPRAGE space and used to calculate regional PET values in the gray and white matter. Tissue probabilities were determined by segmenting each MPRAGE using Unified Segmentation (Ashburner & Friston, 2005) in SPM12 (Wellcome Trust Centre for Neuroimaging, London, UK), with the MCALT tissue priors. Median PET values in each ROI were divided by median uptake in cerebellar crus gray matter (for tau-PET and Aβ-PET) or pons (for FDG-PET) to create standard uptake value ratios (SUVR). Gray matter MRI-volumes were also summed from the SPM12 segmentations for each MCALT atlas ROI. PET images were not partial volume corrected; however the adopted approach of masking atlas regions based on the segmentation avoids outlying voxels that are mostly nontissue, and thus reduces the effects of partial volume. Ninety-two ROIs in the frontal, sensorimotor, temporal, parietal, and occipital lobes and subcortical regions were selected for the statistical analyses. The complete list of these ROIs can be found in Table 2. A global Aβ-SUVR was generated for each patient in the study and a cut-point of 1.42 was used to establish Aβ

TABLE 2 List of ROIs

Frontal	Frontal Sup L
	Frontal Sup R
	Frontal Sup Orb L
	Frontal Sup Orb R
	Frontal Mid L
	Frontal Mid R
	Frontal Mid Orb L
	Frontal Mid Orb R
	Frontal Inf Oper L
	Frontal Inf Oper R
	Frontal Inf Tri L
	Frontal Inf Tri R
	Frontal Inf Orb L
	Frontal Inf Orb R
	Frontal Sup Medial L
	Frontal Sup Medial R
	Frontal Med Orb L
	Frontal Med Orb R
	Rectus L
	Rectus R
	Insula L
	Insula R
	Cingulum Ant L
	Cingulum Ant R
	Cingulum Mid L
	Cingulum Mid R
Sensorimotor	Supp Motor Area L
	Supp Motor Area R
	Precentral L
	Precentral R
	Rolandic Oper L
	Rolandic Oper R
	Postcentral L
	Postcentral R
	Paracentral Lobule L
	Paracentral Lobule R
Medial Temporal	Hippocampus L
	Hippocampus R
	Amygdala L
	Amygdala R
	Fusiform L
	Fusiform R
	Entorhinal Cortex L
	Entorhinal Cortex R
	ParaHippocampal L
	ParaHippocampal R
Lateral Temporal	Heschl L
	Heschl R
	Temporal Sup L
	Temporal Sup R
	Temporal Pole Sup L
	Temporal Pole Sup R

(Continues)

TABLE 2 (Continued)

	Temporal Pole Mid L
	Temporal Pole Mid R
	Temporal Mid L
	Temporal Mid R
	Temporal inf L
	Temporal inf R
Medial Parietal	Precuneus L
	Precuneus R
	Cingulum Post L
	Cingulum Post R
	Retrosplenial Cortex L
	Retrosplenial Cortex R
Lateral Parietal	Parietal Sup L
	Parietal Sup R
	Parietal inf L
	Parietal inf R
	SupraMarginal L
	SupraMarginal R
	Angular L
	Angular R
Medial Occipital	Calcarine L
	Calcarine R
	Cuneus L
	Cuneus R
	Lingual L
	Lingual R
Lateral Occipital	Occipital Sup L
	Occipital Sup R
	Occipital Mid L
	Occipital Mid R
	Occipital inf L
	Occipital inf R
Subcortical	Caudate L
	Caudate R
	Putamen L
	Putamen R
	Pallidum L
	Pallidum R
	Thalamus L
	Thalamus R

positivity (Jack et al., 2017). PET and MR images of each subject were subsequently spatially normalized to the MCALT template and blurred with a 6 and 8 mm full width at half maximum kernel, respectively, for the voxel-based analyses.

The DTI-FA images were processed as described in a previous study (Schwarz et al., 2014). Briefly, DTI-FA images were normalized to a study-specific template using ANTs tools (Avants, Yushkevich, et al., 2010). ROI values were computed using the Johns Hopkins University (JHU) single-subject "Eve" DTI Atlas (Oishi et al., 2008), registered to the study-specific FA template using ANTs. The median DTI-FA scalar values within 49 left and right white matter tract ROIs were measured.

2.4 | Voxel-based morphometry

Full factorial analyses were implemented in SPM12 (Wellcome Trust Centre for Neuroimaging, London, UK) for all the imaging modalities to identify alterations in tau deposition, gray matter volume, glucose metabolism, and fractional anisotropy in the two patient groups (PCA and lvPPA) relative to a cohort of 111 age-matched cognitively normal controls that had been recruited into the Mayo Clinic Study of Aging.

2.5 | Univariate ROI analysis

Partial Pearson's correlations were performed between each pair of modalities (i.e., tau-PET vs. FDG-PET, tau-PET vs. MRI-volume, tau-PET vs. DTI-FA, FDG-PET vs. MRI-volume, FDG-PET vs. DTI-FA, and MRI-volume vs. DTI-FA). Age was modeled as a confounding factor. Because of the large number of correlations (92×92 ROIs or 92×49 ROIs for each map), multiple comparisons correction was necessary to assess their significance. A permutation approach was implemented as described in (Avants, Cook, et al., 2010). Briefly, we randomly permuted 1,000 times one of the two input datasets so that, for several pairs, the data did not come from the same subject. We then recomputed all the correlations for all the permuted datasets and calculated a corrected p-value as the ratio between the number of times the correlation coefficient obtained using the permuted datasets was higher than the one obtained using the original datasets and the number of permutations computed. If the corrected p-value was greater than .05, the correlation was not considered significant. The permutation approach is less strict than the classic Bonferroni method. However, it was appropriate because the Bonferroni's

assumption of independence between statistical tests does not hold true for correlations between ROIs that are spatially close to each other. The statistical analyses were performed in Matlab2018a (The Mathworks, Inc., Natick, MA).

2.6 | Multivariate ROI analysis

SCCA was applied using the penalized multivariate analysis (PMA) R package (Witten et al., 2009) to investigate multivariate relationships between all the combinations of modalities (six possible pairs). In each analysis, a lasso penalty of 0.3 for PET and MRI data and 0.4 for DTI data was assigned to achieve the desired level of sparsity (Adams et al., 2018), that is, to have SCCA selecting sets of regions of sensible sizes. The same permutation approach that was used for the univariate analyses was applied to assess the significance of the canonical dimensions (Avants, Cook, et al., 2010). To display the results, we color-coded the MCALT atlas, assigning a color to the voxels inside the ROIs that were associated to a nonzero canonical weight.

2.7 | Voxel-level multimodal analysis

In order to complement the local correlations in the ROI-based analyses, images from tau-PET, FDG-PET, and MRI (gray matter segmentations) were compared voxel-wise using VoxelStats (Mathotaarachchi et al., 2016), which fits a linear model to datasets consisting of images of different modalities. Age was again modeled as a confounding factor. A Random Field Theory (RFT)-based multiple comparisons correction was applied on the results (Mathotaarachchi et al., 2016) and only
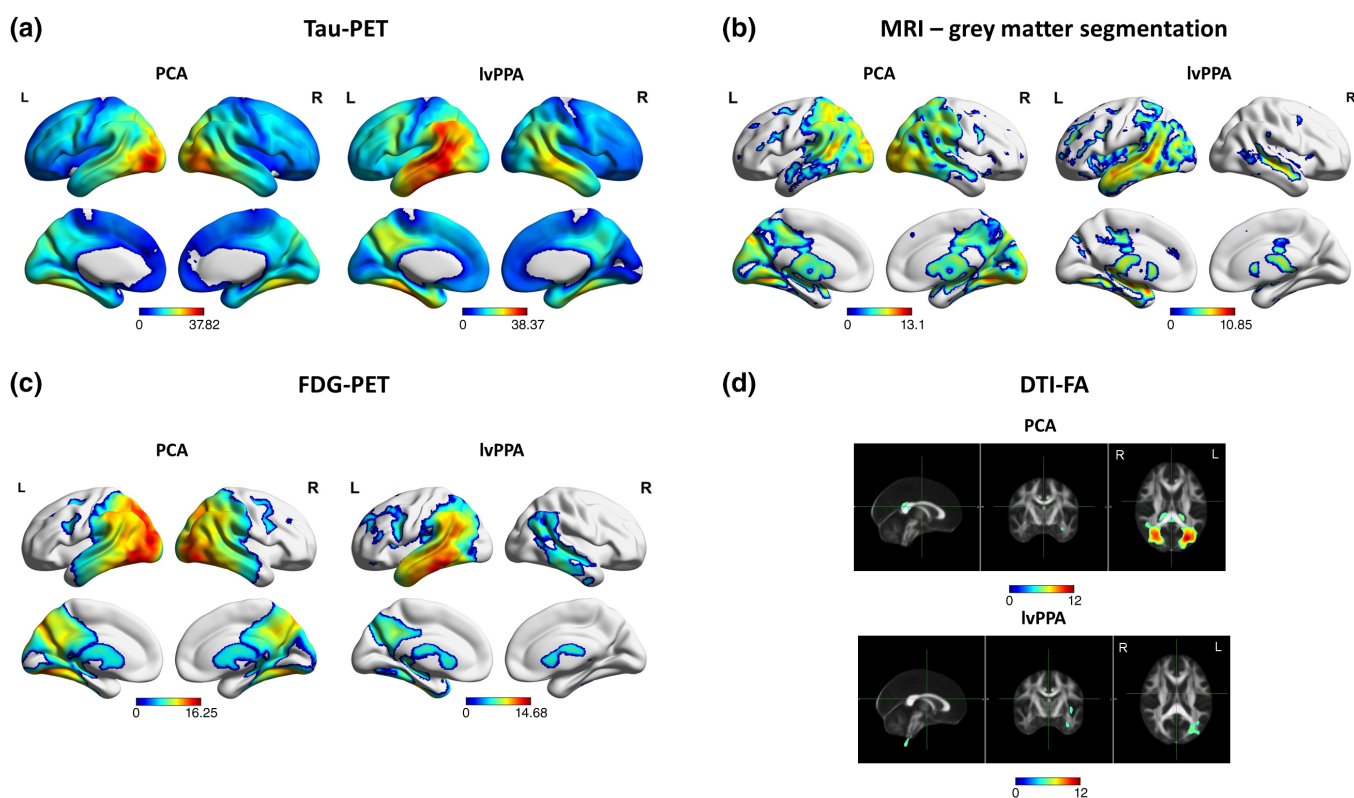
FIGURE 1 SPM maps of increased tau uptake (a), gray matter volume loss (b), hypometabolism (c), and FA reduction (d) for PCA and lvPPA patients in comparison to normal controls. Results are shown after correcting for multiple comparisons (FWE, $p < .05$) [Color figure can be viewed at wileyonlinelibrary.com]

TABLE 3 Canonical weight for each ROI in the first two canonical dimensions for SCCA between FDG-SUVR and tau-SUVR. Canonical weights equal to zero for both variables and dimensions are not listed

	Dimension 1		Dimension 2	
ROI	FDG-SUVR	Tau-SUVR	FDG-SUVR	Tau-SUVR
Frontal_Sup_L	0	0	−0.442	0
Frontal_Sup_Orb_L	0	0	−0.164	0.458
Frontal_Mid_L	0	0	−0.347	0
Frontal_Mid_Orb_L	0	0	−0.406	0.104
Frontal_Inf_Oper_L	0	0	−0.445	0.084
Frontal_Inf_Tri_L	0	0	−0.36	0.415
Frontal_Inf_Orb_L	0	0	−0.293	0.401
Frontal_Sup_Medial_L	0	0	−0.258	0.336
Frontal_Med_Orb_L	0	0	0	0.286
Frontal_Med_Orb_R	0	0	0	0.003
Rectus_L	0	0	0	0.194
Rectus_R	0	0	0	0.003
Cingulum_Ant_L	0	0	0	0.421
Cingulum_Ant_R	0	0	0	0.173
Supp_Motor_Area_L	0	0	−0.095	0
Precentral_R	0	0.078	0	0
Postcentral_R	0	0.016	0	0
Fusiform_R	−0.021	0.022	0	0
Heschl_R	−0.068	0	0	0
Temporal_Sup_R	−0.159	0	0	0
Temporal_Pole_Sup_L	0	0	−0.054	0
Temporal_Pole_Mid_L	0	0	−0.013	0
Temporal_Mid_R	−0.074	0	0	0
Precuneus_L	−0.139	0	0	0
Precuneus_R	−0.547	0.073	0	0
Cingulum_Post_R	−0.023	0	0	0
Parietal_Sup_R	−0.17	0	0	0
Parietal_Inf_R	−0.005	0	0	0
SupraMarginal_R	−0.339	0	0	0
Angular_R	−0.067	0	0	0
Calcarine_L	0	0.236	0	0
Calcarine_R	0	0.478	0	0
Cuneus_L	0	0.141	0	0
Cuneus_R	−0.259	0.444	0	0
Lingual_L	0	0.255	0	0
Lingual_R	−0.091	0.478	0	0
Occipital_Sup_R	−0.488	0.399	0	0
Occipital_Mid_R	−0.428	0.149	0	0
Occipital_Inf_R	0	0.109	0	0

TABLE 4 Canonical weight for each ROI in the first two canonical dimensions for SCCA MRI-volume and tau-SUVR. Canonical weights equal to zero for both variables and dimensions are not listed

	Dimension 1		Dimension 2	
ROI	MRI-volume	Tau-SUVR	MRI-volume	Tau-SUVR
Frontal_Sup_L	0	0	0	0.324
Frontal_Sup_R	0	0.189	0	0
Frontal_Mid_L	0	0	0	0.612
Frontal_Mid_R	0	0.76	0	0
Frontal_Mid_Orb_L	0	0	0	0.069
Frontal_Mid_Orb_R	0	0.091	0	0
Frontal_Inf_Oper_L	0	0	0	0.251
Frontal_Inf_Oper_R	0	0.325	0	0
Frontal_Inf_Tri_L	0	0	0	0.212
Frontal_Inf_Tri_R	0	0.152	0	0
Frontal_Inf_Orb_L	0	0	0	0.077
Cingulum_Mid_L	0	0	0	0.019
Supp_Motor_Area_L	0	0	0	0.07
Supp_Motor_Area_R	0	0.099	0	0
Precentral_R	0	0.308	0	0
Postcentral_R	0	0.145	0	0
Fusiform_R	−0.163	0	0	0
Temporal_Sup_L	0	0	−0.409	0
Temporal_Mid_L	0	0	−0.478	0
Temporal_Mid_R	−0.311	0	−0.271	0
Temporal_Inf_L	0	0	−0.238	0
Temporal_Inf_R	−0.316	0	−0.11	0
Precuneus_L	0	0	−0.367	0.223
Precuneus_R	−0.442	0.023	0	0
Cingulum_Post_L	0	0	−0.439	0.325
Cingulum_Post_R	0	0.033	0	0.106
Retrosplenial_Cortex_L	0	0	−0.347	0.462
Retrosplenial_Cortex_R	0	0.215	−0.09	0
Parietal_Sup_L	−0.173	0	−0.026	0
Parietal_Sup_R	−0.441	0	0	0
Parietal_Inf_R	−0.432	0.205	−0.041	0
SupraMarginal_R	−0.165	0.083	0	0
Angular_L	−0.062	0	−0.061	0.126
Angular_R	−0.374	0.02	0	0
Cuneus_R	0	0.135	0	0
Occipital_Sup_R	0	0.094	0	0

the voxels that survived the correction are shown. VoxelStats analyses were not performed between MRI or PET and DTI-FA, because there is not a voxel-to-voxel correspondence between the white matter tracts and the regions of gray and white matter assessed by the other modalities.

3 | RESULTS

3.1 | Voxel-based morphometry

Figure 1 shows increased tau uptake (a), gray matter volume loss (b), hypometabolism (c), and FA reduction (d) for PCA and lvPPA patients in comparison to normal controls. Results are shown after correcting for multiple comparisons (FWE, $p < .05$). Both the PCA and lvPPA patients showed an increased uptake of tau-PET tracer in the parietal regions (Figure 1a). Additionally, the tau signal was more elevated in the occipital regions for PCA patients and more prominent on the left side for lvPPA patients (Figure 1a). Similar patterns were observed for gray matter loss (Figure 1b) and hypometabolism (Figure 1c). Both patient groups showed decreased FA in the posterior regions of the brain (Figure 1d), although with more striking findings in PCA.

3.2 | Multimodal analyses

In the following sections, we present the results from the multimodal analyses conducted on the whole cohort of patients. Only partial Pearson's correlations that survived the permutation test are shown

TABLE 5 Canonical weight for each ROI in the first two canonical dimensions for SCCA between FDG-SUVR and MRI-volume. Canonical weights equal to zero for both variables and dimensions are not listed

ROI	Dimension 1		Dimension 2	
	FDG-SUVR	MRI-volume	FDG-SUVR	MRI-volume
Precentral_R	0	0	0.442	0
Rolandic_Oper_R	0	0	0.236	0
Postcentral_R	0.288	0	0	0
Fusiform_R	0.331	0.275	0	0.297
Entorhinal_Cortex_R	0	0	0.026	0
ParaHippocampal_R	0	0	0.433	0
Temporal_Inf_R	0	0.024	0.086	0.08
Precuneus_R	0.265	0	0	0
Cingulum_Post_R	0.111	0	0	0
Retrosplenial_Cortex_R	0.051	0	0.009	0
Parietal_Sup_L	0	0	0.16	0
Parietal_Sup_R	0.384	0	0	0
Parietal_Inf_R	0	0.206	0.264	0.245
SupraMarginal_R	0.178	0.416	0	0.434
Angular_L	0	0.08	0	0
Angular_R	0	0.385	0.212	0.302
Cuneus_L	0	0.02	0	0.105
Cuneus_R	0	0.327	0.456	0.44
Lingual_R	0	0.13	0.437	0.241
Occipital_Sup_L	0	0	0.117	0
Occipital_Sup_R	0.438	0.097	0	0.149
Occipital_Mid_L	0	0.143	0	0.001
Occipital_Mid_R	0.47	0.611	0	0.528
Occipital_Inf_R	0.36	0.163	0	0.057

TABLE 6 Canonical weight for each ROI in the first canonical dimension for SCCA between FDG-SUVR and white matter tract DTI-FA. Canonical weights equal to zero are not listed

ROI	Dimension 1	
	FDG-SUVR	DTI-FA
Hippocampus_R	0.518	–
Amygdala_R	0.303	–
Fusiform_R	0.441	–
Entorhinal_Cortex_R	0.366	–
ParaHippocampal_R	0.431	–
Precuneus_R	0.086	–
Cingulum_Post_R	0.044	–
Retrosplenial_Cortex_R	0.067	–
SupraMarginal_R	0.06	–
Cuneus_L	0.056	–
Cuneus_R	0.043	–
Lingual_L	0.242	–
Occipital_Sup_L	0.009	–
Occipital_Mid_R	0.21	–
PTR_L	–	0.32
PTR_R	–	0.49
CGC_L	–	0.078
CGC_R	–	0.269
CGH_L	–	0.069
CGH_R	–	0.394
SS_L	–	0.166
SS_R	–	0.493
MCP_R	–	0.001
Fx	–	0.179
SCC	–	0.34

in the maps and discussed in the text. Similarly, only canonical dimensions that were significant after the permutation test are discussed and their canonical weights are reported in Tables 3–6 for each ROI. The VoxelStats maps are reported after the RFT correction for multiple comparisons. Partial Pearson's correlation maps and significant SCCA canonical dimensions are reported separately for the PCA and lvPPA groups in Supporting Information (Supporting Information Figures S1–S4, Supporting Information Tables S1–S4), but discussed below.

3.3 | Tau multimodal relationships

Tau-SUVR showed strong negative regional relationships with both FDG-SUVR and MRI-volume (i.e., increased tau was associated with decreased metabolism and volume) (Figure 2a,b). The strongest associations between tau deposition and FDG metabolism were observed between increased tau in the occipital lobes and decreased metabolism in the parietal and occipital lobes, and between increased tau and decreased metabolism in the frontal lobes (Figure 2a). The first two dimensions from the SCCA (Figure 3) supported these associations, with the first dimension reflecting the occipital associations and the second dimension the frontal associations (Figure 3a). Local correlations in the parietal and occipital lobes were observed for both the PCA and lvPPA patients, when analyzed separately, but were more evident in PCA (Supporting Information Figures S1a and S2a). The frontal lobe revealed local correlations only for lvPPA (Supporting

Information Figure S2a). Tau showed negative associations with MRI-volume in the occipital lobe, although the strongest relationships were observed between increased tau across frontal, sensorimotor, parietal and occipital lobes, and decreased volume in the lateral temporoparietal lobes (Figure 2b). The first two dimensions of the SCCA both involved frontal and parietal regions for tau and temporoparietal regions for MRI-volume, although Dimension 1 was mainly right lateralized and Dimension 2 was more bilateral or left lateralized (Figure 3b). Analogous, although weaker, associations were noted in the two groups, when analyzed separately, without clear differences in asymmetry (Supporting Information Figures S1b and S2b).

Two opposite trends were observed for the relationship between tau and white matter tract DTI-FA (Figure 2c): increased tau in the posterior part of the brain (sensorimotor, parietal and occipital regions) was associated to decreased DTI-FA of the splenium of the corpus callosum, posterior thalamic radiation, cingulum and right sagittal striatum, and increased tau in the posterior part of the brain was associated to increased DTI-FA of the internal and external capsule. The SCCA performed on tau-SUVR and DTI-FA did not survive the permutation test. While the associations between tau-SUVR and DTI-FA in the PCA patients were very similar to the ones found for the whole cohort (Supporting Information Figure S1c), the lvPPA patients showed some differences, with more negative associations between
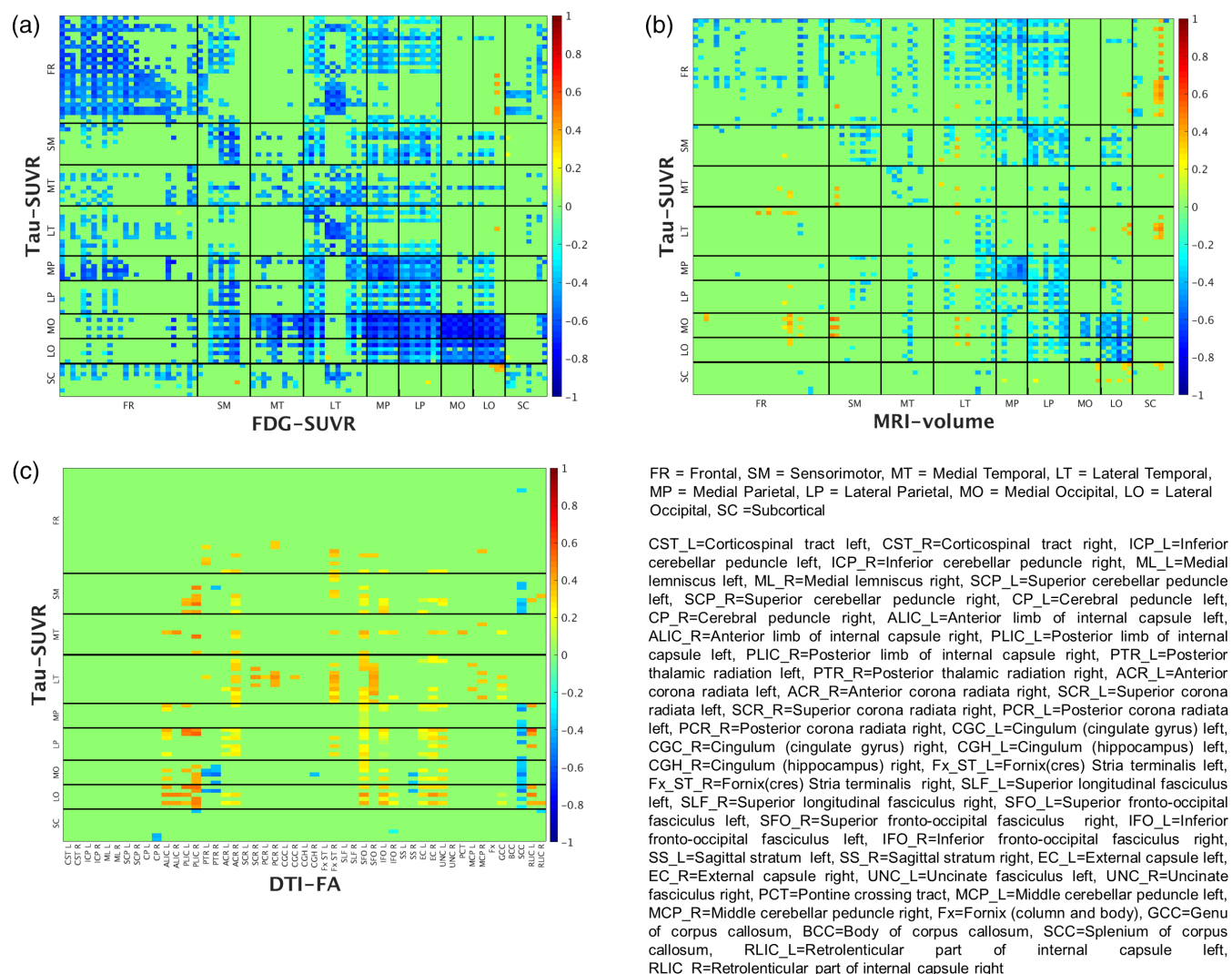
FIGURE 2 Pearson's partial correlation coefficients corrected for age for tau-SUVR versus FDG-SUVR (a), MRI-volume (b), and white matter tract DTI-FA (c). A negative correlation with FDG-SUVR, MRI-volume or DTI-FA is a correlation in the "expected" direction, that is, increased tau associated with hypometabolism, atrophy, or reduced white matter FA. Correlations that did not survive the permutation test were set to zero [Color figure can be viewed at wileyonlinelibrary.com]

frontal tau and white matter tracts that are located in the frontal and temporal lobes (Supporting Information Figure S2c).

The VoxelStats maps (Figure 4) largely confirmed the strongest local relationship shown in the correlation maps. A negative relationship between tau-PET and FDG-PET uptake was present mostly within voxels in the occipital (superior and middle occipital, cuneus, calcarine, lingual), frontal (superior, middle and inferior), sensorimotor (rolandic operculum, precentral), medial parietal (precuneus), and lateral temporal (inferior and middle temporal) bilateral regions (Figure 4a). The negative relationships between tau-PET uptake and gray matter MRI-volume were less widespread but also involved the occipital lobe (superior, middle and inferior occipital, cuneus, lingual), bilaterally with an emphasis on the right side (Figure 4b), and also the frontal (middle, inferior) and medial parietal (retrosplenial cortex) regions (not visible in the slice shown in Figure 4b). The VoxelStats analyses performed on the PCA and lvPPA groups separately revealed hardly any association, possibly because of the lack of statistical power due to the small samples.

3.4 | Neurodegeneration multimodal relationships

Regional associations between FDG-SUVR and MRI-volume were strong (Figure 5a) and supported by SCCA (Figure 6a). Specifically, hypometabolism and atrophy were locally positively correlated in the frontal, parietal and occipital regions. More distant relationships were also present with medial temporal atrophy associated with widespread hypometabolism, and frontal hypometabolism associated with widespread atrophy. The first two dimensions of the SCCA included parietal and occipital regions for both modalities (Figure 6a). VoxelStats confirmed the diffuse bilateral positive association between FDG-PET uptake and gray matter MRI-volume (Figure 4c), with the strongest associations in parietal (precuneus, retrosplenial cortex) and occipital (superior, middle and inferior occipital, lingual, cuneus) regions, followed by frontal (superior, middle and inferior frontal, cingulum), sensorimotor (precentral, paracentral lobule), and medial temporal (hippocampus) regions. Analyzing the two groups separately, we observed weaker local frontal, parietal, and occipital correlations in both the PCA and the lvPPA group, when compared with the whole
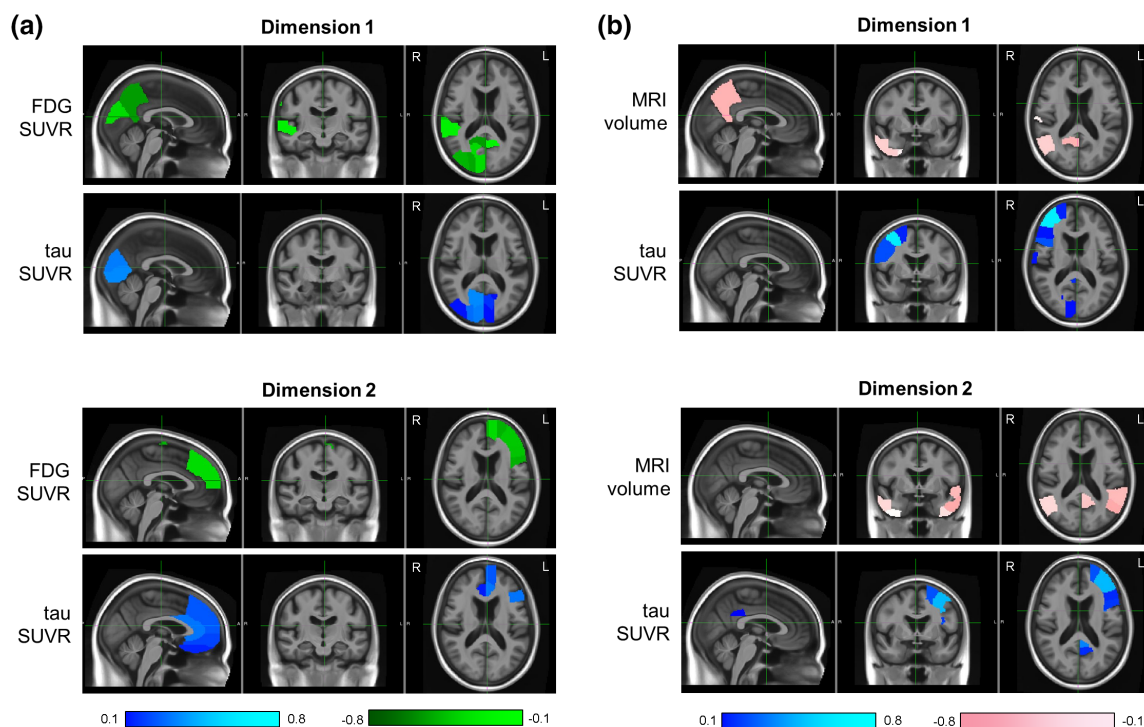
FIGURE 3 First and second canonical dimensions from sparse canonical correlation analyses between tau-SUVR and FDG-SUVR (a) and between tau-SUVR and MRI-volume (b). Colors represent the canonical weights found by SCCA for the ROIs that contributed to the canonical dimensions. ROIs associated to weights less than 0.1 are left transparent [Color figure can be viewed at wileyonlinelibrary.com]

cohort (Supporting Information Figures S3a and S4a). The distant relationship between medial temporal atrophy and widespread hypometabolism was present in PCA (Supporting Information Figure S3a), while the distant relationship between frontal hypometabolism and widespread atrophy was present in both groups, although more weakly in lvPPA (Supporting Information Figure S4a).
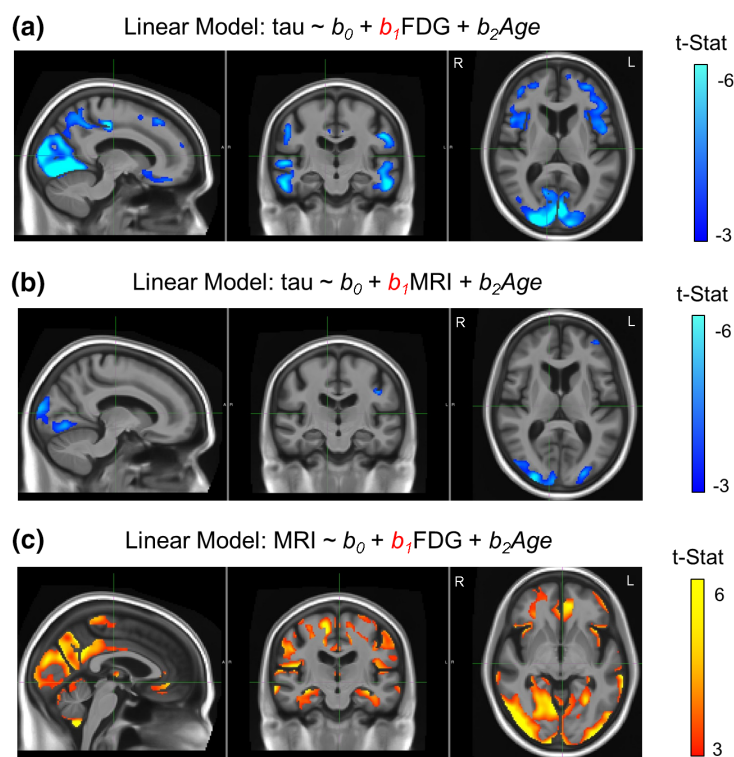
FIGURE 4 T-statistical maps generated with VoxelStats showing voxel-level correlations between tau-PET and FDG-PET (a); tau-PET and MRI (b); MRI and FDG-PET (c). Age was used as a confounding factor. Results are shown after correction for multiple comparisons (cluster-based RFT, $p < .001$) [Color figure can be viewed at wileyonlinelibrary.com]
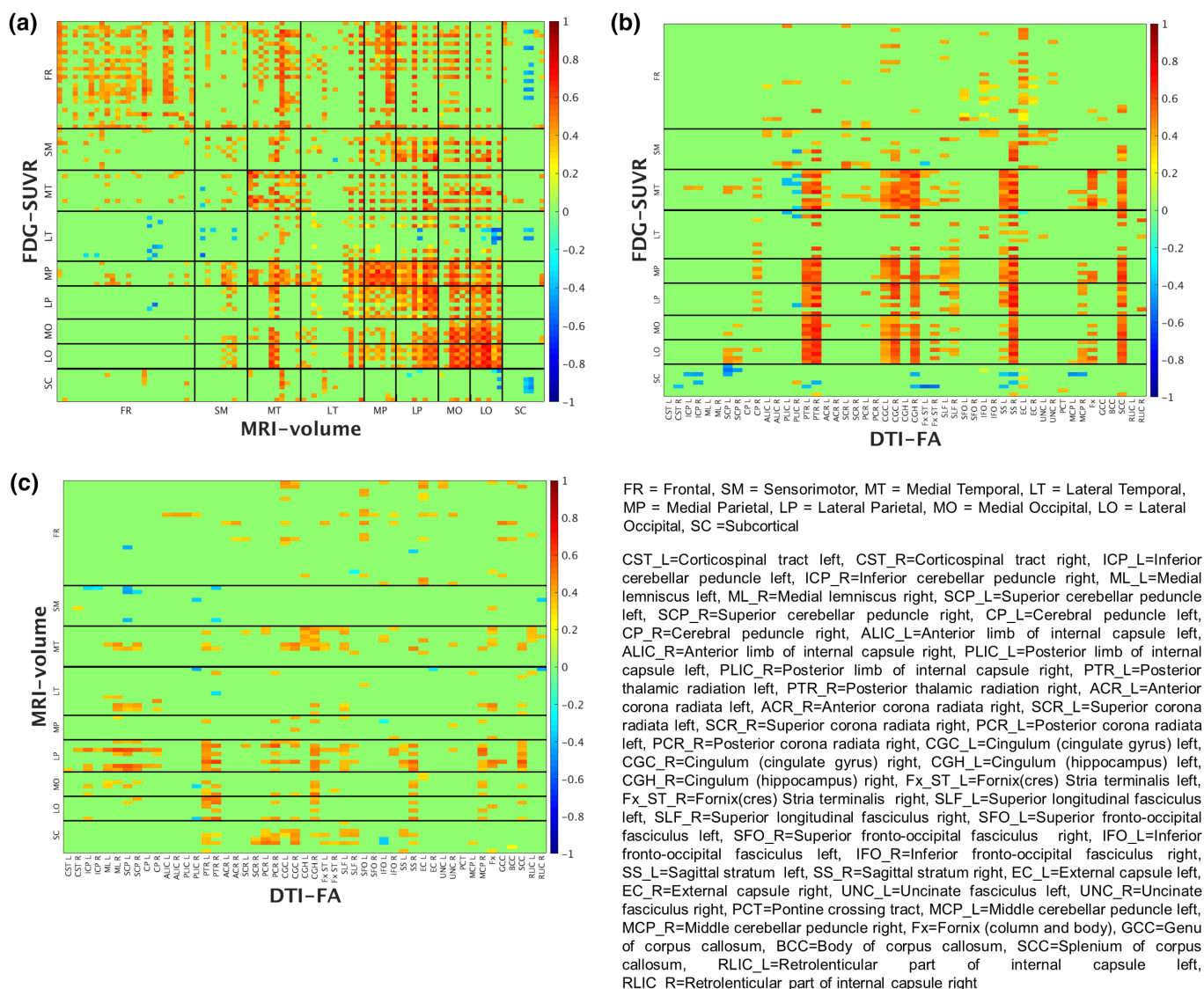
FIGURE 5 Pearson's partial correlation coefficients corrected for age for FDG-SUVR versus MRI-volume (a), FDG-SUVR versus white matter tract DTI-FA (b), and MRI-volume versus white matter tract DTI-FA (c). A positive correlation between FDG-SUVR, MRI-volume or DTI-FA means a correlation in the "expected" direction. Correlations that did not survive the permutation test were set to zero [Color figure can be viewed at wileyonlinelibrary.com]

FR = Frontal, SM = Sensorimotor, MT = Medial Temporal, LT = Lateral Temporal, MP = Medial Parietal, LP = Lateral Parietal, MO = Medial Occipital, LO = Lateral Occipital, SC =Subcortical

CST_L=Corticospinal tract left, CST_R=Corticospinal tract right, ICP_L=Inferior cerebellar peduncle left, ICP_R=Inferior cerebellar peduncle right, ML_L=Medial lemniscus left, ML_R=Medial lemniscus right, SCP_L=Superior cerebellar peduncle left, SCP_R=Superior cerebellar peduncle right, CP_L=Cerebral peduncle left, CP_R=Cerebral peduncle right, ALIC_L=Anterior limb of internal capsule left, ALIC_R=Anterior limb of internal capsule right, PLIC_L=Posterior limb of internal capsule left, PLIC_R=Posterior limb of internal capsule right, PTR_L=Posterior thalamic radiation left, PTR_R=Posterior thalamic radiation right, ACR_L=Anterior corona radiata left, ACR_R=Anterior corona radiata right, SCR_L=Superior corona radiata left, SCR_R=Superior corona radiata right, PCR_L=Posterior corona radiata left, PCR_R=Posterior corona radiata right, CGC_L=Cingulum (cingulate gyrus) left, CGC_R=Cingulum (cingulate gyrus) right, CGH_L=Cingulum (hippocampus) left, CGH_R=Cingulum (hippocampus) right, Fx_ST_L=Fornix(cres) Stria terminalis left, Fx_ST_R=Fornix(cres) Stria terminalis right, SLF_L=Superior longitudinal fasciculus left, SLF_R=Superior longitudinal fasciculus right, SFO_L=Superior fronto-occipital fasciculus left, SFO_R=Superior fronto-occipital fasciculus right, IFO_L=Inferior fronto-occipital fasciculus left, IFO_R=Inferior fronto-occipital fasciculus right, SS_L=Sagittal stratum left, SS_R=Sagittal stratum right, EC_L=External capsule left, EC_R=External capsule right, UNC_L=Uncinate fasciculus left, UNC_R=Uncinate fasciculus right, PCT=Pontine crossing tract, MCP_L=Middle cerebellar peduncle left, MCP_R=Middle cerebellar peduncle right, Fx=Fornix (column and body), GCC=Genu of corpus callosum, BCC=Body of corpus callosum, SCC=Splenium of corpus callosum, RLIC_L=Retrolenticular part of internal capsule left, RLIC_R=Retrolenticular part of internal capsule right

The relationship between white matter tract DTI-FA and FDG-SUVR (Figures 5b and 6b) or MRI-volume (Figure 5c) were both mostly positive, with decreased DTI-FA associated with hypometabolism and atrophy. Medial temporal, parietal, and occipital hypometabolism was associated with decreased DTI-FA in the posterior thalamic radiation, cingulum, sagittal stratum, and splenium of the corpus callosum (Figure 5b). These relationships were captured in the first dimension of SCCA (Figure 6b). The second dimension of SCCA between FDG-SUVR and DTI-FA did not survive the permutation test. Similar associations were noted in the PCA group, while the lvPPA group did not show many relevant associations (Supporting Information Figures S3b and S4b). Lateral parietal atrophy was positively correlated to decreased DTI-FA in several white matter tracts such as the posterior thalamic radiation, internal capsule, and splenium of the corpus callosum (Figure 5c), although the SCCA did not survive the permutation test. The PCA group showed the same trends as the whole cohort, while the lvPPA group did not show any clear pattern, except

for greater involvement of frontal volumes (Supporting Information Figures S3c and S4c).

4 | DISCUSSION

This study investigated multimodal relationships between tau deposition, hypometabolism, gray matter atrophy, and white matter tract degeneration in atypical AD. To do so, we implemented complementary univariate and multivariate statistical approaches, both ROI- and voxel-based, using tau-PET and FDG-PET images, MRI and fractional anisotropy DTI collected in a population of 40 atypical AD patients, presenting with either PCA or lvPPA clinical phenotype. We showed that, in atypical AD, tau deposition (as measured by [18F]AV-1451 PET uptake) has a close relationship to neurodegeneration and therefore it is likely a crucial player in determining regional patterns of atrophy and, particularly, hypometabolism. We also showed that damage
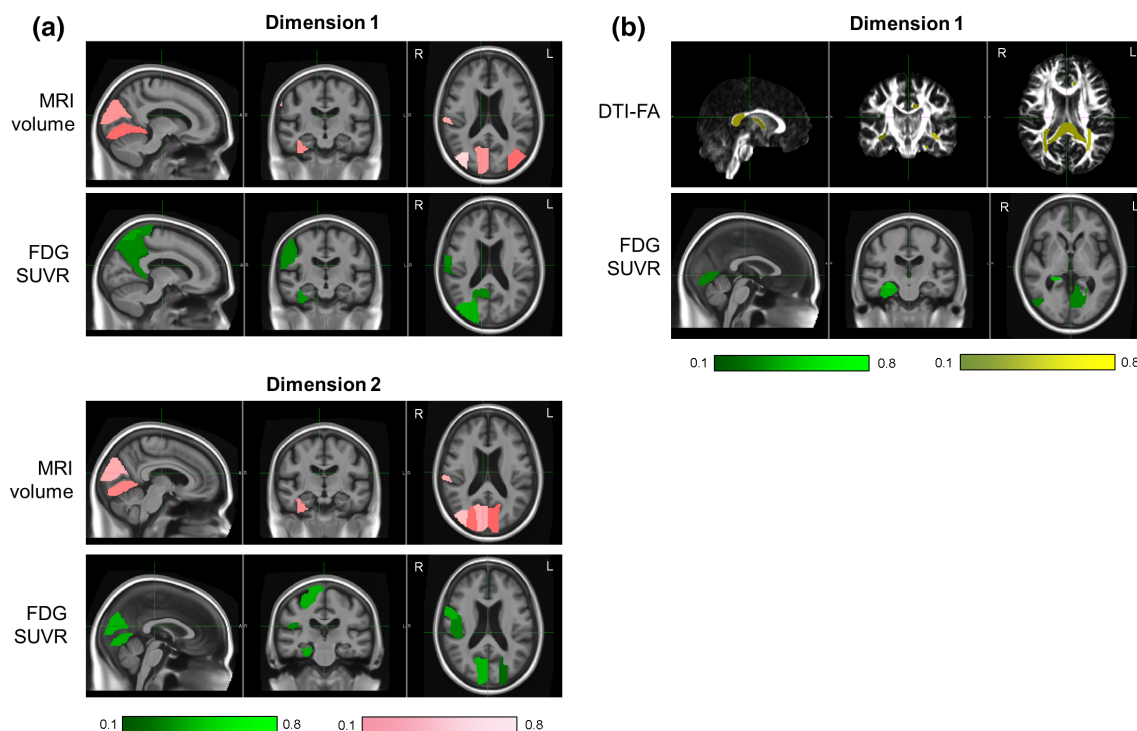
FIGURE 6 First and second canonical dimensions from sparse canonical correlation analysis between FDG-SUVR and MRI-volume (a) and between FDG-SUVR and white matter tract DTI-FA (b—Second dimension did not survive permutation test). Colors represent the canonical weights found by SCCA for the ROIs that contributed to the canonical dimensions. ROIs associated to weights less than 0.1 are left transparent [Color figure can be viewed at wileyonlinelibrary.com]

in a specific network of white matter tracts is related to tau uptake and neurodegeneration.

Tau uptake measured on [18F]AV-1451 showed strong regional associations with both hypometabolism and atrophy, with correlations particularly high locally, that is, within a lobe, as another study observed in a cohort of AD patients (Iaccarino et al., 2018). Specifically, we found strong correlations between tau deposition and both hypometabolism and atrophy in the occipital lobes, as well as between tau deposition and hypometabolism in the frontal lobes across the atypical AD cohort. This finding is in agreement with the topology of neurodegeneration in atypical AD, where both the frontal and occipital lobes can be affected (Gorno-Tempini et al., 2011; Madhavan et al., 2013; Singh et al., 2015; Tang-Wai et al., 2004; Whitwell et al., 2007, 2013). In general, we found that tau tracer uptake was associated more strongly with hypometabolism than with atrophy, as we observed in our previous study (Whitwell et al., 2018). In addition, while the strongest associations between tau and hypometabolism were local, we observed more diffuse and distant relationships between tau and atrophy, with temporoparietal atrophy correlating with tau deposition in the frontoparietal lobes. This regional disconnection may support the notion that MRI-atrophy occurs further in time from the tau deposition, compared with hypometabolism. It could also suggest that tau-PET and FDG-PET are more sensitive indicators of the respective underlying abnormality than atrophy on MRI is, therefore, the correlations were stronger, or that PET scans are methodologically consistent and therefore correlate better with each other (Whitwell et al., 2018). Interestingly, SCCA performed on tau-PET and MRI-volumes and on tau-PET and FDG-PET uptakes selected

mostly bilateral or right regions in the first canonical dimension and mostly left regions in the second canonical dimension. This likely reflects the fact that tau uptake and neurodegeneration in atypical AD subjects can be asymmetric (Tetzloff et al., 2018). In contrast, tau deposition was only mildly related to the degeneration of white matter tracts. Specifically, the presence of tau in the posterior regions of the brain was connected to a reduced fractional anisotropy in a set of tracts that connect to these regions, including the splenium of the corpus callosum, and in tracts that connect posterior regions of the brain to the thalamus (i.e., posterior thalamic radiation and sagittal striatum). The corpus callosum, cingulum and posterior thalamic radiations have previously been shown to be involved in atypical AD (Caso et al., 2015; Madhavan et al., 2016), and our findings further suggest that degeneration of these tracts may be related to tau deposition. The relationships between tau and white matter tract degeneration were, however, relatively weak. We also observed a few tracts in which increased tau was associated with less degeneration, suggesting caution in interpreting these relationships. The positive associations between tau and fractional anisotropy could reflect the fact that the internal and external capsule were relatively spared in our atypical AD cohort and remain unaffected as tau uptake increases, although we cannot rule out potential methodological confounds.

Gray matter volumes from MRI revealed strong local associations with FDG-PET uptake in the frontal, parietal and occipital lobes, suggesting that atrophy and hypometabolism are deeply interconnected in AD (Chetelat et al., 2016), as we might expect. Distant associations were also present: specifically, frontal hypometabolism was related to temporal, parietal and occipital atrophy, and medial temporal atrophy

was related to widespread hypometabolism. This suggests a particularly high sensitivity of FDG to frontal abnormalities and of MRI to medial temporal abnormalities in atypical AD and that optimum regional biomarkers from FDG-PET and MRI may differ. It also suggests that frontal hypometabolism and medial temporal atrophy may be late features of the disease, given that patients with these features already have widespread cortical neurodegeneration. The markers of neurodegeneration, particularly hypometabolism, showed strong correlations with white matter tract degeneration. The relationships of white matter tract degeneration with tau and FDG uptake presented several similarities. They were in the same direction, that is, lower fractional anisotropy corresponded to more tau deposition and lower metabolism, and they involved similar white matter tracts, such as the splenium of corpus callosum, cingulum, posterior thalamic radiation and sagittal striatum, and brain regions, such as the parietal and occipital lobe. However, white matter tract degeneration showed a stronger relationship with hypometabolism than with tau deposition or atrophy. This may support a Wallerian degeneration model of white matter tract degeneration, where reduced FA results from reduced metabolism in the neuron, rather than directly from tau deposition in the axon. Indeed, in AD, tau deposition occurs primarily in the form of neurofibrillary tangles which are found in the neuron. Although we selected fractional anisotropy as a marker of white matter tract degeneration, the same findings (not shown) held true for mean diffusivity.

When the two clinical variants of atypical AD (PCA and lvPPA) were analyzed separately, their multimodal associations were similar to those of the whole cohort. However, they were generally weaker, with most SCCA not surviving the permutation test, likely because of the smaller sample sizes. For the associations between tau-SUVR and FDG-SUVR, we observed strong local correlations in both groups, similar to the whole group patterns. However, these analyses suggested that local correlations in the occipital lobe were driven mainly by PCA, while the local correlations in the frontal lobe were driven by lvPPA. The occipital lobe did show the most striking tau uptake and hypometabolism in PCA in the voxel-based morphometry analysis, as expected, but the frontal lobe was not the most affected region in lvPPA, begging the question of why this region showed the strongest local correlations between tau and hypometabolism. Other multimodal relationships, such as between tau uptake and DTI-FA and between MRI-volume and DTI-FA, were also observed in the frontal lobe in lvPPA. These findings could suggest that we have captured the lvPPA group at a phase in the disease where tau deposition and neurodegeneration is actively occurring in the frontal lobes, perhaps having spread from an earlier focus in the temporoparietal cortex. This hypothesis is, however, difficult to prove without longitudinal data. Generally, the results we obtained in the whole group for multimodal relationships between DTI-FA and the other metrics better mirrored the findings in PCA, with weaker and less focal associations observed in lvPPA. The lvPPA group also showed less striking patterns of white matter degeneration in the voxel-based morphometry maps, as we have previously found in an independent sample (Madhavan et al., 2016). We could conclude from this that white matter tract degeneration is a more prominent feature of PCA, or involves a more homogeneous set of white matter tracts in PCA, compared with lvPPA. Interestingly, the

local multimodal relationships between MRI-volume and FDG-SUVR were strong in the whole cohort but much weaker for the two groups analyzed separately, perhaps because of the smaller sample size or because the range of data is truncated when analyzing the separate, more homogeneous, clinical variants. Although the separate analyses of the two clinical phenotypes are informative, the benefits of merging them into one larger cohort (n = 40) are a better range in the data and increased power, therefore a higher confidence in our conclusions.

Regional associations between PET SUVR and MRI volumes raise the methodological question on the utility and impact of partial volume correction (PVC). In this study, we analyzed the data both with and without two-compartment PVC (Meltzer, Leal, Mayberg, Wagner, & Frost, 1990), and the results were qualitatively the same. Because PVC did not affect our main PET findings, we concluded that they were not driven by the presence or absence of atrophy. We decided to show results without PVC in order to keep our PET and MRI analyses relatively methodologically independent of each other and avoid adding unnecessary correlations between these channels of information. Regarding the statistical methods we used, the SCCA produced results that were largely equivalent to the correlation maps. However, SCCA provided some advantages in terms of interpretability of the results: its multivariate nature allowed looking at relationships between imaging modalities in an overarching way, and its sparsity constraint selected only a compact set of ROIs that significantly impacted those relationships. In addition, the SCCA were less computationally expensive than the univariate analyses. To summarize, SCCA proved to be an effective and efficient methodology to identify the regions of the brain that are associated to each other between modalities. A limitation of the study is that, with a different lasso penalty, we would have obtained potentially different results. In fact, depending on how the sparse parameter is selected, one will either have more distributed or more selective regions (Avants, Cook, et al., 2010). Additionally, one could employ different lasso penalties for each SCCA input variable. We adopted this approach only for the analyses that involved DTI, since the number of white matter tracts (49) was smaller than the number of PET and MRI ROIs (92). In the rest of the analyses, we used the same penalty for both PET/MRI input variables for simplicity and consistency. In this study, we adopted a two-view SCCA approach in order to compare the results to those obtained with the univariate technique. However, multi-view SCCA algorithms are available to relate more than two imaging modalities to each other. For the most part, voxel-wise analyses confirmed the local relationships between modalities. Since the number of ROIs is obviously smaller than the number of voxels, ROI-based analyses were less computationally expensive than VoxelStats analyses, despite including both local and distant statistical tests.

We used cross-sectional analyses to uncover *spatial* relationships between protein accumulation and neurodegeneration in atypical AD. Although some imaging modalities revealed overlapping patterns (e.g., strong local associations between tau uptake and hypometabolism) that could be interpreted as duplicative information, the abundancy of distant multimodal relationships suggests that the different modalities offer rather complementary information on the complex pathology of atypical AD. According to the current understanding of AD, Aβ deposition begins years, if not decades, before the clinical

symptoms of cognitive decline, which are directly caused by neurodegeneration, and tau accumulation happens in between the two (Jack et al., 2013; Quiroz et al., 2018). Therefore, the natural continuation of this research will be to gather longitudinal data and integrate the current findings with the *temporal* associations between protein accumulation, atrophy, hypometabolism, and white matter disruption.

In summary, our study elucidated significant spatial pathophysiological relationships between protein deposition (tau), neurodegeneration (hypometabolism, atrophy), and structural connectivity networks (white matter tract fractional anisotropy) involved in atypical AD. These findings could have important consequences for selecting imaging biomarkers as outcome measures in clinical trials and even in the development of new therapeutic strategies for atypical AD.

ORCID

Irene Sintini https://orcid.org/0000-0001-6845-0735
Christopher G. Schwarz https://orcid.org/0000-0002-1466-8357

REFERENCES

Adams, J. N., Lockhart, S. N., Li, L., & Jagust, W. J. (2018). Relationships between tau and glucose metabolism reflect Alzheimer's disease pathology in cognitively Normal older adults. *Cerebral Cortex*. https://doi.org/10.1093/cercor/bhy078

Ashburner, J., & Friston, K. J. (2005). Unified segmentation. *NeuroImage*, 26(3), 839–851. https://doi.org/10.1016/j.neuroimage.2005.02.018

Avants, B. B., Cook, P. A., Ungar, L., Gee, J. C., & Grossman, M. (2010). Dementia induces correlated reductions in white matter integrity and cortical thickness: A multivariate neuroimaging study with sparse canonical correlation analysis. *NeuroImage*, 50(3), 1004–1016. https://doi.org/10.1016/j.neuroimage.2010.01.041

Avants, B. B., Epstein, C. L., Grossman, M., & Gee, J. C. (2008). Symmetric diffeomorphic image registration with cross-correlation: Evaluating automated labeling of elderly and neurodegenerative brain. *Medical Image Analysis*, 12(1), 26–41. https://doi.org/10.1016/j.media.2007.06.004

Avants, B. B., Libon, D. J., Rascovsky, K., Boller, A., McMillan, C. T., Massimo, L., … Grossman, M. (2014). Sparse canonical correlation

analysis relates network-level atrophy to multivariate cognitive measures in a neurodegenerative population. *NeuroImage*, 84, 698–711. https://doi.org/10.1016/j.neuroimage.2013.09.048

Avants, B. B., Yushkevich, P., Pluta, J., Minkoff, D., Korczykowski, M., Detre, J., & Gee, J. C. (2010). The optimal template effect in hippocampus studies of diseased populations. *NeuroImage*, 49(3), 2457–2466. https://doi.org/10.1016/j.neuroimage.2009.09.062

Balasa, M., Gelpi, E., Antonell, A., Rey, M. J., Sanchez-Valle, R., Molinuevo, J. L., … Neurological Tissue Bank/University of Barcelona/-Hospital Clínic NTB/UB/HC Collaborative Group. (2011). Clinical features and APOE genotype of pathologically proven early-onset Alzheimer disease. *Neurology*, 76(20), 1720–1725. https://doi.org/10.1212/WNL.0b013e31821a44dd

Bischof, G. N., Jessen, F., Fliessbach, K., Dronse, J., Hammes, J., Neumaier, B., … Alzheimer's Disease Neuroimaging Imaging. (2016). Impact of tau and amyloid burden on glucose metabolism in Alzheimer's disease. *Annals of Clinical Translational Neurology*, 3(12), 934–939. https://doi.org/10.1002/acn3.339

Braak, H., & Braak, E. (1991). Neuropathological staging of Alzheimer-related changes. *Acta Neuropathologica*, 82(4), 239–259.

Caso, F., Agosta, F., Mattavelli, D., Migliaccio, R., Canu, E., Magnani, G., … Filippi, M. (2015). White matter degeneration in atypical Alzheimer disease. *Radiology*, 277(1), 162–172. https://doi.org/10.1148/radiol.2015142766

Chetelat, G., Ossenkoppele, R., Villemagne, V. L., Perrotin, A., Landeau, B., Mezenge, F., … Rabinovici, G. D. (2016). Atrophy, hypometabolism and clinical trajectories in patients with amyloid-negative Alzheimer's disease. *Brain*, 139, 2528–2539. https://doi.org/10.1093/brain/aww159

Cope, T. E., Rittman, T., Borchert, R. J., Jones, P. S., Vatansever, D., Allinson, K., … Rowe, J. B. (2018). Tau burden and the functional connectome in Alzheimer's disease and progressive supranuclear palsy. *Brain*, 141, 550–567. https://doi.org/10.1093/brain/awx347

Crutch, S. J., Lehmann, M., Schott, J. M., Rabinovici, G. D., Rossor, M. N., & Fox, N. C. (2012). Posterior cortical atrophy. *Lancet Neurology*, 11(2), 170–178. https://doi.org/10.1016/S1474-4422(11)70289-7

Dronse, J., Fliessbach, K., Bischof, G. N., von Reutern, B., Faber, J., Hammes, J., … Drzezga, A. (2017). In vivo patterns of tau pathology, amyloid-beta burden, and neuronal dysfunction in clinical variants of Alzheimer's disease. *Journal of Alzheimer's Disease*, 55(2), 465–471. https://doi.org/10.3233/JAD-160316

Galantucci, S., Tartaglia, M. C., Wilson, S. M., Henry, M. L., Filippi, M., Agosta, F., … Gorno-Tempini, M. L. (2011). White matter damage in primary progressive aphasias: A diffusion tensor tractography study. *Brain*, 134(Pt 10), 3011–3029. https://doi.org/10.1093/brain/awr099

Galton, C. J., Patterson, K., Xuereb, J. H., & Hodges, J. R. (2000). Atypical and typical presentations of Alzheimer's disease: A clinical, neuropsychological, neuroimaging and pathological study of 13 cases. *Brain*, 123, 484–498. https://doi.org/10.1093/brain/123.3.484

Gorno-Tempini, M. L., Brambati, S. M., Ginex, V., Ogar, J., Dronkers, N. F., Marcone, A., … Miller, B. L. (2008). The logopenic/phonological variant of primary progressive aphasia. *Neurology*, 71(16), 1227–1234. https://doi.org/10.1212/01.wnl.0000320506.79811.da

Gorno-Tempini, M. L., Hillis, A. E., Weintraub, S., Kertesz, A., Mendez, M., Cappa, S. F., … Grossman, M. (2011). Classification of primary progressive aphasia and its variants. *Neurology*, 76(11), 1006–1014. https://doi.org/10.1212/WNL.0b013e31821103e6

Hoenig, M. C., Bischof, G. N., Seemiller, J., Hammes, J., Kukolja, J., Onur, O. A., … Drzezga, A. (2018). Networks of tau distribution in Alzheimer's disease. *Brain*, 141, 568–581. https://doi.org/10.1093/brain/awx353

Hotelling, H. (1936). Relations between two sets of variates. *Biometrika*, 28(3/4), 321–377.

Iaccarino, L., Tammewar, G., Ayakta, N., Baker, S. L., Bejanin, A., Boxer, A. L., … Rabinovici, G. D. (2018). Local and distant relationships between amyloid, tau and neurodegeneration in Alzheimer's disease. *Neuroimage: Clinical*, 17, 452–464. https://doi.org/10.1016/j.nicl.2017.09.016

Jack, C. R., Jr., Knopman, D. S., Jagust, W. J., Petersen, R. C., Weiner, M. W., Aisen, P. S., … Trojanowski, J. Q. (2013). Tracking pathophysiological processes in Alzheimer's disease: An updated hypothetical model of dynamic biomarkers. *Lancet Neurology*, 12(2), 207–216. https://doi.org/10.1016/S1474-4422(12)70291-0

Jack, C. R., Jr., Lowe, V. J., Senjem, M. L., Weigand, S. D., Kemp, B. J., Shiung, M. M., ... Petersen, R. C. (2008). 11C PiB and structural MRI provide complementary information in imaging of Alzheimer's disease and amnestic mild cognitive impairment. *Brain*, 131(Pt 3), 665–680. https://doi.org/10.1093/brain/awm336

Jack, C. R., Wiste, H. J., Weigand, S. D., Therneau, T. M., Lowe, V. J., Knopman, D. S., ... Petersen, R. C. (2017). Defining imaging biomarker cut points for brain aging and Alzheimer's disease. *Alzheimer's & Dementia*, 13(3), 205–216. https://doi.org/10.1016/j.jalz.2016.08.005

Jones, D. T., Graff-Radford, J., Lowe, V. J., Wiste, H. J., Gunter, J. L., Senjem, M. L., ... Jack, C. R. (2017). Tau, amyloid, and cascading network failure across the Alzheimer's disease spectrum. *Cortex*, 97, 143–159. https://doi.org/10.1016/j.cortex.2017.09.018

La Joie, R., Perrotin, A., Barre, L., Hommet, C., Mezenge, F., Ibazizene, M., ... Chetelat, G. (2012). Region-specific hierarchy between atrophy, hypometabolism, and beta-amyloid (a beta) load in Alzheimer's disease dementia. *Journal of Neuroscience*, 32(46), 16265–16273. https://doi.org/10.1523/Jneurosci.2170-12.2012

Madhavan, A., Schwarz, C. G., Duffy, J. R., Strand, E. A., Machulda, M. M., Drubach, D. A., ... Whitwell, J. L. (2016). Characterizing white matter tract degeneration in Syndromic variants of Alzheimer's disease: A diffusion tensor imaging study. *Journal of Alzheimer's Disease*, 49(3), 633–643. https://doi.org/10.3233/Jad-150502

Madhavan, A., Whitwell, J. L., Weigand, S. D., Duffy, J. R., Strand, E. A., Machulda, M. M., ... Josephs, K. A. (2013). FDG PET and MRI in logopenic primary progressive aphasia versus dementia of the Alzheimer's type. *PLoS One*, 8(4), e62471. https://doi.org/10.1371/journal.pone.0062471

Mahoney, C. J., Malone, I. B., Ridgway, G. R., Buckley, A. H., Downey, L. E., Golden, H. L., ... Warren, J. D. (2013). White matter tract signatures of the progressive aphasias. *Neurobiology of Aging*, 34(6), 1687–1699. https://doi.org/10.1016/j.neurobiolaging.2012.12.002

Mathotaarachchi, S., Wang, S. Q., Shin, M., Pascoal, T. A., Benedet, A. L., Kang, M. S., ... Neuroimaging, A. s. D. (2016). VoxelStats: A MATLAB package for multi-modal voxel-wise brain image analysis. *Frontiers in Neuroinformatics*, 10, 20. https://doi.org/10.3389/fninf.2016.00020

Meltzer, C. C., Leal, J. P., Mayberg, H. S., Wagner, H. N., & Frost, J. J. (1990). Correction of pet data for partial volume effects in human cerebral-cortex by Mr imaging. *Journal of Computer Assisted Tomography*, 14(4), 561–570. https://doi.org/10.1097/00004728-199007000-00011

Migliaccio, R., Agosta, F., Possin, K. L., Rabinovici, G. D., Miller, B. L., & Gorno-Tempini, M. L. (2012). White matter atrophy in Alzheimer's disease variants. *Alzheimers Dement*, 8(5 Suppl), S78–S87 e71-72. https://doi.org/10.1016/j.jalz.2012.04.010

Nasrallah, I. M., Chen, Y. J., Hsieh, M. K., Phillips, J. S., Ternes, K., Stockbower, G. E., ... Wolk, D. A. (2018). (18)F-Flortaucipir PET/MRI correlations in nonamnestic and amnestic variants of Alzheimer disease. *Journal of Nuclear Medicine*, 59(2), 299–306. https://doi.org/10.2967/jnumed.117.194282

Oishi, K., Zilles, K., Amunts, K., Faria, A., Jiang, H. Y., Li, X., ... Mori, S. (2008). Human brain white matter atlas: Identification and assignment of common anatomical structures in superficial white matter. *NeuroImage*, 43(3), 447–457. https://doi.org/10.1016/j.neuroimage.2008.07.009

Ossenkoppele, R., Schonhaut, D. R., Baker, S. L., O'Neil, J. P., Janabi, M., Ghosh, P. M., ... Rabinovici, G. D. (2015). Tau, amyloid, and hypometabolism in a patient with posterior cortical atrophy. *Annals of Neurology*, 77(2), 338–342. https://doi.org/10.1002/ana.24321

Ossenkoppele, R., Schonhaut, D. R., Scholl, M., Lockhart, S. N., Ayakta, N., Baker, S. L., ... Rabinovici, G. D. (2016). Tau PET patterns mirror clinical and neuroanatomical variability in Alzheimer's disease. *Brain*, 139(Pt 5), 1551–1567. https://doi.org/10.1093/brain/aww027

Quiroz, Y. T., Sperling, R. A., Norton, D. J., Baena, A., Arboleda-Velasquez, J. F., Cosio, D., ... Johnson, K. A. (2018). Association between amyloid and tau accumulation in young adults with autosomal dominant Alzheimer disease. *JAMA Neurology*, 75(5), 548–556. https://doi.org/10.1001/jamaneurol.2017.4907

Rabinovici, G. D., Jagust, W. J., Furst, A. J., Ogar, J. M., Racine, C. A., Mormino, E. C., ... Gorno-Tempini, M. L. (2008). Abeta amyloid and glucose metabolism in three variants of primary progressive aphasia. *Annals of Neurology*, 64(4), 388–401. https://doi.org/10.1002/ana.21451

Schwarz, C. G., Reid, R. I., Gunter, J. L., Senjem, M. L., Przybelski, S. A., Zuk, S. M., ... Alzheimer's Disease Neuroimaging Initiative. (2014). Improved DTI registration allows voxel-based analysis that outperforms tract-based spatial statistics. *NeuroImage*, 94, 65–78. https://doi.org/10.1016/j.neuroimage.2014.03.026

Singh, T. D., Josephs, K. A., Machulda, M. M., Drubach, D. A., Apostolova, L. G., Lowe, V. J., & Whitwell, J. L. (2015). Clinical, FDG and amyloid PET imaging in posterior cortical atrophy. *Journal of Neurology*, 262(6), 1483–1492. https://doi.org/10.1007/s00415-015-7732-5

Tang-Wai, D. F., Graff-Radford, N. R., Boeve, B. F., Dickson, D. W., Parisi, J. E., Crook, R., ... Petersen, R. C. (2004). Clinical, genetic, and neuropathologic characteristics of posterior cortical atrophy. *Neurology*, 63(7), 1168–1174. https://doi.org/10.1212/01.Wnl.0000140289.18472.15

Tetzloff, K. A., Graff-Radford, J., Martin, P. R., Tosakulwong, N., Machulda, M. M., Duffy, J. R., ... Whitwell, J. L. (2018). Regional distribution, asymmetry, and clinical correlates of tau uptake on [18F]AV-1451 PET in atypical Alzheimer's disease. *Journal of Alzheimer's Disease*, 62(4), 1713–1724. https://doi.org/10.3233/JAD-170740

Whitwell, J. L., Dickson, D. W., Murray, M. E., Weigand, S. D., Tosakulwong, N., Senjem, M. L., ... Josephs, K. A. (2012). Neuroimaging correlates of pathologically defined subtypes of Alzheimer's disease: A case-control study. *Lancet Neurology*, 11(10), 868–877. https://doi.org/10.1016/S1474-4422(12)70200-4

Whitwell, J. L., Graff-Radford, J., Tosakulwong, N., Weigand, S. D., Machulda, M. M., Senjem, M. L., ... Drubach, D. A. (2018). Imaging correlations of tau, amyloid, metabolism, and atrophy in typical and atypical Alzheimer's disease. *Alzheimer's & Dementia*, 14, 1005–1014.

Whitwell, J. L., Jack, C. R., Jr., Kantarci, K., Weigand, S. D., Boeve, B. F., Knopman, D. S., ... Josephs, K. A. (2007). Imaging correlates of posterior cortical atrophy. *Neurobiology of Aging*, 28(7), 1051–1061. https://doi.org/10.1016/j.neurobiolaging.2006.05.026

Whitwell, J. L., Jack, C. R., Przybelski, S. A., Parisi, J. E., Senjem, M. L., Boeve, B. F., ... Josephs, K. A. (2011). Temporoparietal atrophy: A marker of AD pathology independent of clinical diagnosis. *Neurobiology of Aging*, 32(9), 1531–1541. https://doi.org/10.1016/j.neurobiolaging.2009.10.012

Whitwell, J. L., Lowe, V. J., Duffy, J. R., Strand, E. A., Machulda, M. M., Kantarci, K., ... Josephs, K. A. (2013). Elevated occipital beta-amyloid deposition is associated with widespread cognitive impairment in logopenic progressive aphasia. *Journal of Neurology, Neurosurgery, and Psychiatry*, 84(12), 1357–1364. https://doi.org/10.1136/jnnp-2013-305628

Wirth, M., Bejanin, A., La Joie, R., Arenaza-Urquijo, E. M., Gonneaud, J., Landeau, B., ... Chetelat, G. (2018). Regional patterns of gray matter volume, hypometabolism, and beta-amyloid in groups at risk of Alzheimer's disease. *Neurobiology of Aging*, 63, 140–151. https://doi.org/10.1016/j.neurobiolaging.2017.10.023

Witten, D. M., Tibshirani, R., & Hastie, T. (2009). A penalized matrix decomposition, with applications to sparse principal components and canonical correlation analysis. *Biostatistics*, 10(3), 515–534. https://doi.org/10.1093/biostatistics/kxp008

Xia, C., Makaretz, S. J., Caso, C., McGinnis, S., Gomperts, S. N., Sepulcre, J., ... Dickerson, B. C. (2017). Association of in vivo [18F]AV-1451 tau PET imaging results with cortical atrophy and symptoms in typical and atypical Alzheimer disease. *JAMA Neurology*, 74(4), 427–436. https://doi.org/10.1001/jamaneurol.2016.5755

SUPPORTING INFORMATION

Additional supporting information may be found online in the Supporting Information section at the end of the article.